

Vertical Strain-Induced Modification of the Electrical and Spin Properties of Monolayer MoSi_2X_4 ($\text{X} = \text{N}, \text{P}, \text{As}$ and Sb)

Shoeib Babaei Touski

Department of Electrical Engineering, Hamedan University of Technology, Hamedan, Iran

Nayereh Ghobadi*

Department of Electrical Engineering, University of Zanjan, Zanjan, Iran

(Dated: June 15, 2021)

In this work, the electrical and spin properties of monolayer MoSi_2X_4 ($\text{X} = \text{N}, \text{P}, \text{As}$, and Sb) under vertical strain are investigated. The band structures state that MoSi_2N_4 is an indirect semiconductor, whereas other compounds are direct semiconductors. The vertical strain has been selected to modify the electrical properties. The bandgap shows a maximum and decreases for both tensile and compressive strains. The valence band at K-point displays a large spin-splitting, whereas the conduction band has a negligible splitting. On the other hand, the second conduction band has a large spin-splitting and moves down under vertical strain which leads to a large spin-splitting in both conduction and valence bands edges. The projected density of states along with the projected band structure clarifies the origin of these large spin-splittings. These three spin-splittings can be controlled by vertical strain.

PACS numbers:

I. INTRODUCTION

The graphene, the first member of two-dimensional (2D) materials, with honeycomb structure does not exhibit an electronic band gap¹. This problem has motivated the researchers to explore and design novel two-dimensional semiconductors, such as the transition metal dichalcogenides², black phosphorene³, antimonene⁴ and indium selenide⁵. Therefore, exploring new 2D materials with proper electronic properties for particular applications is highly demanded.

After monolayer TMDC, 2D transition metal nitride (TMN) have been proposed in the recent years⁶⁻⁸. Since TMNs do not contain layered structures, the fabrication of large-area TMNs monolayers has remained challenging. Recently, MoSi_2N_4 monolayer based on TMN and without 3D counterpart structure has been synthesized⁹. MoSi_2N_4 is constructed from a MoN_2 monolayer sandwiched between two Si-N monolayers. By analyzing MoSi_2N_4 monolayer, it can be realized that with sandwiching a TMDC-type MZ_2 monolayer into InSe-type A_2Z_2 , twelve different structures with MA_2Z_4 formula have been achieved. They demonstrate different phases such as semiconductor, topological insulators, and Ising superconductors¹⁰. Monolayer MoSi_2N_4 has been successfully fabricated using chemical vapor deposition with large size of up to $15\text{mm} \times 15\text{mm}$ ⁹. This compound demonstrates high strength and excellent stability at ambient. MoSi_2N_4 compound also shows an elastic constant three times larger than monolayer MoS_2 . In addition, the large electron and hole mobility is estimated to be $270/1200 \text{ cm}^2/\text{Vs}$ that is four to six times higher than MoS_2 ones. This high mobility along with outstanding stability in the ambient environment makes this material a promising candidate for future applications.

Other members of MoSi_2N_4 family with MA_2Z_4 for-

mula ($\text{M} = \text{Transition metal}$, $\text{A} = \text{Si}, \text{Ge}$ and $\text{Z} = \text{N}, \text{P}, \text{As}$) have been extensively investigated^{10,11}. These monolayers exhibit a wide range from semiconducting to metallic properties. In addition, some compounds with magnetic transition metal elements also represent magnetic properties¹². The MoSi_2N_4 and WSi_2N_4 monolayers also show high lattice thermal conductivity for thermoelectric applications^{13,14}. Monolayer MoSi_2N_4 and its family also have suitable band gaps up to 1.73eV for potential optical applications in the visible range^{15,16}.

It has been anticipated that MoSi_2N_4 family compounds have a pair of valley pseudospins similar to monolayer MoS_2 ¹⁷. These monolayers have been also predicted to exceed monolayer MoS_2 due to fascinating valleytronic properties, for instance, multiple-folded valleys in monolayer MoSi_2As_4 . The lack of inversion symmetry along with strong spin-orbit coupling from transition metal elements in the MA_2Z_4 family results in two inequivalent valleys (K and K') with sizable spin-splitting and spin-valley coupling¹⁸. For example, WSi_2N_4 demonstrates a large spin-splitting at both conduction and valence bands at K and K'-valleys together with spin-valley coupling.

It has been confirmed theoretically and experimentally that a semiconductor to metal transition occurs in multilayer MoS_2 by applying vertical strain¹⁹⁻²¹. Totally, the decrease of interlayer distance may lead to charge redistribution and semiconductor to metal transition. The out-of-plane strain is presented as a powerful tool to tune the electrical properties of bilayer MA_2Z_4 family²². For instance, the bandgap of bilayer MoSi_2N_4 decreases with increasing compressive strain and the bandgap closes at the strain of 22%. Such a semiconductor to metal transition also occurs in other MA_2Z_4 bilayers¹¹. The transition pressure is distributed from 2.18 GPa in CrSi_2N_4 to 32.04 GPa in TiSi_2N_4 . In another work, the biaxial strain is used to tune the band gaps of bilayer MoSi_2N_4

and WSi_2N_4 ²³. It has been reported that these compounds demonstrate a direct bandgap at compressive strain. Furthermore, it has been shown that strain can also modify the electronic and magnetic properties of VSi_2P_4 monolayer²⁴. The strain increasing changes the phase of this monolayer from a ferromagnetic metal to a spin-gapless semiconductor, afterward to a ferromagnetic semiconductor, and then come back to spin-gapless semiconductor and finally to a ferromagnetic half-metal.

In this work, the effects of vertical strain on the electrical and spin properties of monolayer MoSi_2X_4 ($\text{X}=\text{N}, \text{P}, \text{As}, \text{and Sb}$) are investigated. First, the electrical properties such as bandgap, effective mass, and band edge locations are obtained at equilibrium. In the following, vertical strain is applied to all materials, and the variation of band gaps, band edges, and charge densities are explored. Finally, spin-splitting at both equilibrium and strained samples is studied.

II. COMPUTATIONAL DETAILS

In order to investigate the electrical and spin properties of MoSi_2X_4 ($\text{X}=\text{N}, \text{P}, \text{As}$ and Sb) monolayers, density functional calculations are performed using the SIESTA package²⁵. The generalized gradient approximation (GGA) with the Perdew-Burke-Ernzerhof (PBE)²⁶ functional is employed for the exchange-correlation term. We have adopted fully relativistic pseudopotentials and have taken into account the effect of spin-orbit coupling (SOC). A Monkhorst-Pack k-point grid of $21 \times 21 \times 1$ is chosen for the unit-cell. The energy cutoff is set to be 200 Ry and a double- ζ plus polarization basis-set is used. The total energy is converged to better than 10^{-5} eV and the geometries are fully relaxed until the force on each atom is less than 0.02 eV/Å. A vacuum region of 30 Å is added to avoid interactions in the normal direction. To visualize the atomic structures, XCrySDen package has been used²⁷. The out-of-plane strain is defined as $\varepsilon = (t - t_0)/t_0$, where t_0 and t are the equilibrium and deformed compound thickness, respectively. The effective masses are calculated by using the following equation^{28,29},

$$m^* = \hbar^2 / (\partial^2 E / \partial k^2) \quad (1)$$

Here, \hbar is the reduced Planck constant, E and k are the energy and wave vector of conduction band minimum and valence band maximum.

III. RESULTS AND DISCUSSION

The schematic of the studied compounds is shown in Fig. 1. As it is obvious, a MoN_2 monolayer is sandwiched between two SiN monolayers. The unsaturated Si atoms in SiN sub-layer bond with unsaturated N atoms in MoN_2 . The structural and mechanical properties of

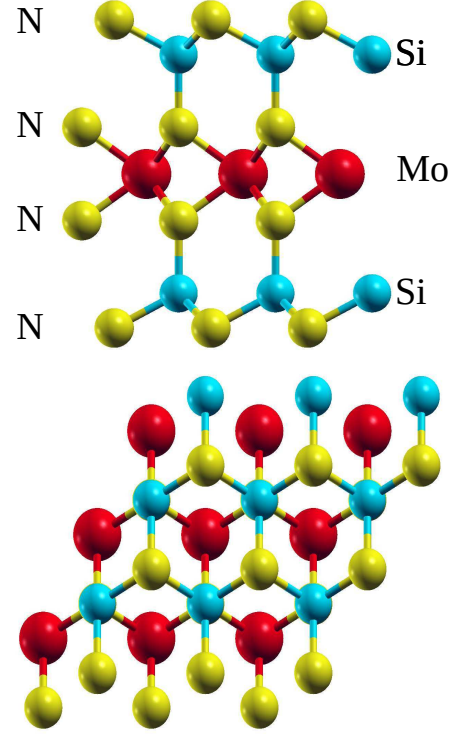


FIG. 1: The schematic of the studied materials with MoSi_2X_4 formula. The atomic structure of MoSi_2N_4 is depicted. N atoms are replaced by P, As and Sb in other studied structures.

four monolayers are presented in Table I. The lattice constant of MoSi_2N_4 is 2.928 Å that is close to experimental result⁹. The lattice constants of MoSi_2P_4 and MoSi_2As_4 are also 3.486 and 3.633 Å, respectively, that are compatible with previous studies^{18,24}. The lattice constant increases for the compounds with heavier X elements. This behavior can be observed in the Mo-X bond length ($d_{\text{Mo-X}}$) in MoX_2 sub-layer, Si-X bond length, and buckling height of SiN sub-layer. Thickness of these compounds demonstrates a high value of 7.119 for MoSi_2N_4 to 10.991 Å for MoSi_2Sb_4 . This high thickness confirms that applying vertical strain is feasible for these compounds. The elastic constants C_{11} and C_{12} are also obtained and reported in the table which is compatible with previously reported amounts¹⁶. These materials are stable and the elastic constants satisfy the Born criteria stability, $0 < C_{11}$, $0 < C_{22}$, $C_{12} < C_{11}$ and $C_{12} < C_{22}$. In addition, the stability of these compounds is studied by phonon dispersion, see Fig. 2. The positive frequencies confirm the stability of these structures.

The two-dimensional contour plots of the first Brillouin zone for the valence and conduction bands are depicted in Fig. 3. The conduction band minimum (CBM) is located at K-valley for all compounds. In the case of MoSi_2N_4 , K-valley approximately demonstrates isotropic contour in different directions whereas, anisotropic behavior is obvious for the other compounds. The anisotropy of K-valley

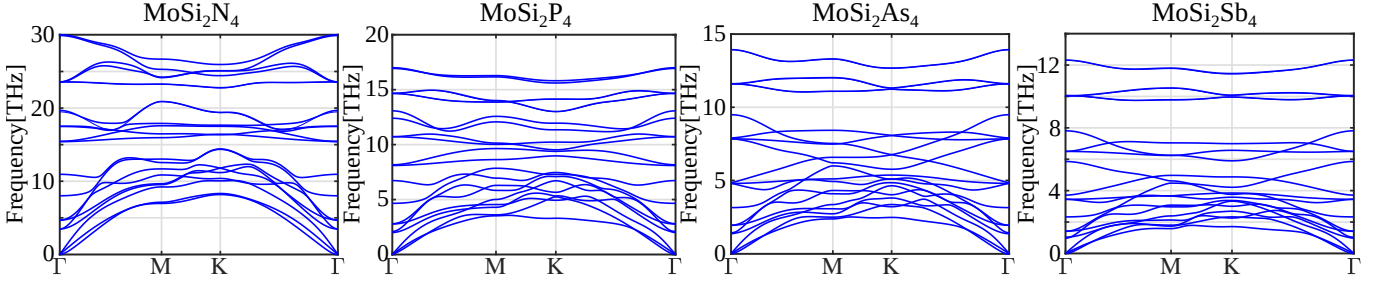


FIG. 2: Phonon dispersion relations for four compounds.

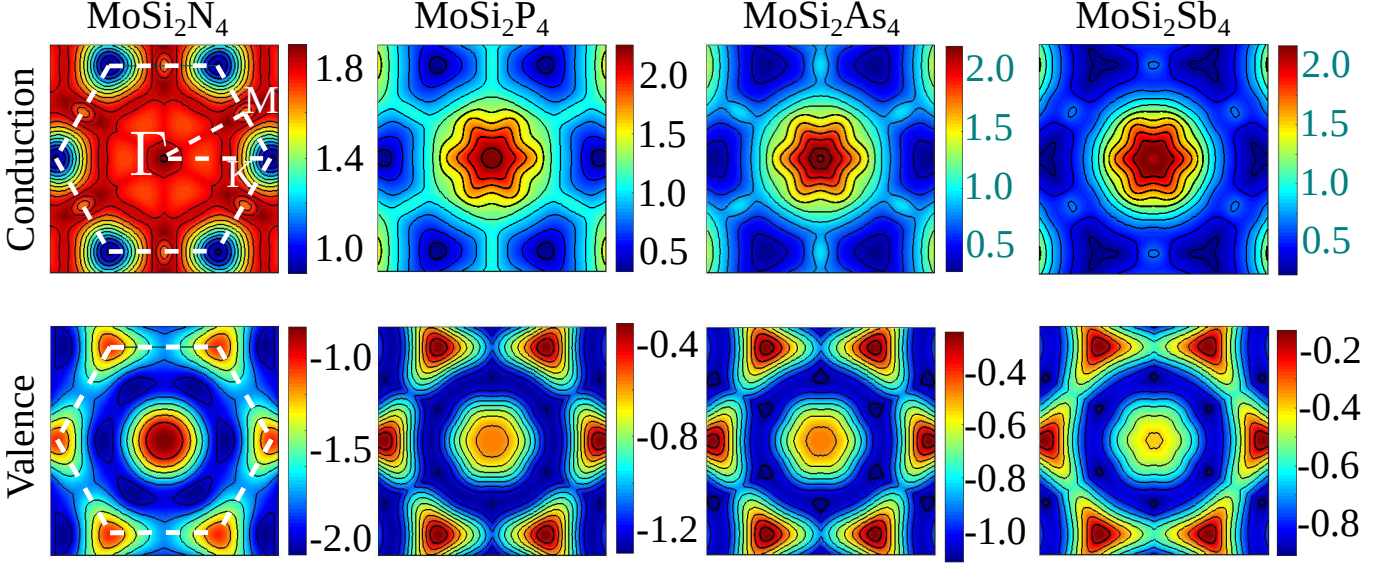


FIG. 3: Two-dimensional map of the conduction and valence bands for all compounds. The first Brillouin zone is indicated for MoSi_2N_4 as a sample. Top and down rows are for the first conduction and valence bands, respectively.

increases for heavier compounds and MoSi_2Sb_4 demonstrates the highest anisotropy. At the same time, the valence band maximum (VBM) is located at Γ -point in the case of MoSi_2N_4 , whereas the energy of K-point is close to the Γ -point. On the other hand, the VBM of other structures is placed at K-point. MoSi_2N_4 demonstrates isotropic contours around Γ -point whereas the other compounds exhibit anisotropic behavior. However, K-point in the valence band shows a high anisotropy with triangular contours for all compounds.

The band structures of the four studied materials are drawn in Fig. 4. MoSi_2N_4 demonstrates an indirect bandgap from Γ -valley in the valence to K-valley in the conduction band whereas, K-point at the valence band is close to Γ -point and contributes to the top of the valence band. Three other compounds have a direct bandgap at K-point. In these compounds, Γ -point at valence band also is close to K-point. On the other hand, K-point displays a considerable spin-splitting whereas, the splitting vanishes for Γ -point due to the high symmetry. The minimum of the second conduction band with a large spin-splitting is near to the minimum of the first band. In order to further analyze the electronic properties of

the structures, the projected density of states (PDOS) is also depicted in Fig. 4. The states near the VBM and CBM are mainly contributed by the Mo atom. X atoms also contribute to the conduction and valence bands, but their contributions are lower than the Mo atom.

The electrical and spin properties of four materials are summarized in Table II. First, the band gaps with and without spin-orbit coupling consideration are compared. In the case of MoSi_2N_4 , the band gaps without and with SOC are approximately the same. These values which are in good agreement with experimental work⁹, are 1.73 and 1.721 eV, respectively. The bandgap of MoSi_2P_4 without(with) SOC is 0.772(0.648) eV that is near to 0.61 eV reported for with SOC¹⁸. The bandgap of MoSi_2As_4 decreases from 0.664 to 0.525 eV with applying spin-orbit coupling, while the values of 0.6 eV and 0.41-0.5 eV are reported for without and with spin-orbit coupling consideration, respectively^{9,18,24,30}. The SOC has more significant effects on the heavier compounds so that the bandgap reduces by 0.172 eV for MoSi_2Sb_4 with applying SOC. In addition, the conduction and valence band maximum is presented in the table. In the end, the spin-splitting at K-point in the valence band,

TABLE I: The lattice constant (a), the Mo-X (d_{Mo-X}) and Si-X (d_{Si-X}) bond lengths, the vertical distance between Si and X atoms (Δ_{Si-X}), the thickness and the elastic constants (C_{11} and C_{12}) of $MoSi_2X_4$ monolayers.

	$a(\text{\AA})$	$d_{Mo-X}(\text{\AA})$	$d_{Si-X}(\text{\AA})$	$\Delta_{Si-X}(\text{\AA})$	Thickness(\AA)	$C_{11}(\text{N/m})$	$C_{12}(\text{N/m})$
$MoSi_2N_4$	2.928	2.111	1.763	0.531	7.119	472.66	142.02
$MoSi_2P_4$	3.486	2.477	2.253	1.046	9.486	207.77	58.46
$MoSi_2As_4$	3.633	2.583	2.366	1.136	10.021	178.03	54.75
$MoSi_2Sb_4$	3.898	2.777	2.589	1.278	10.991	141.40	47.72

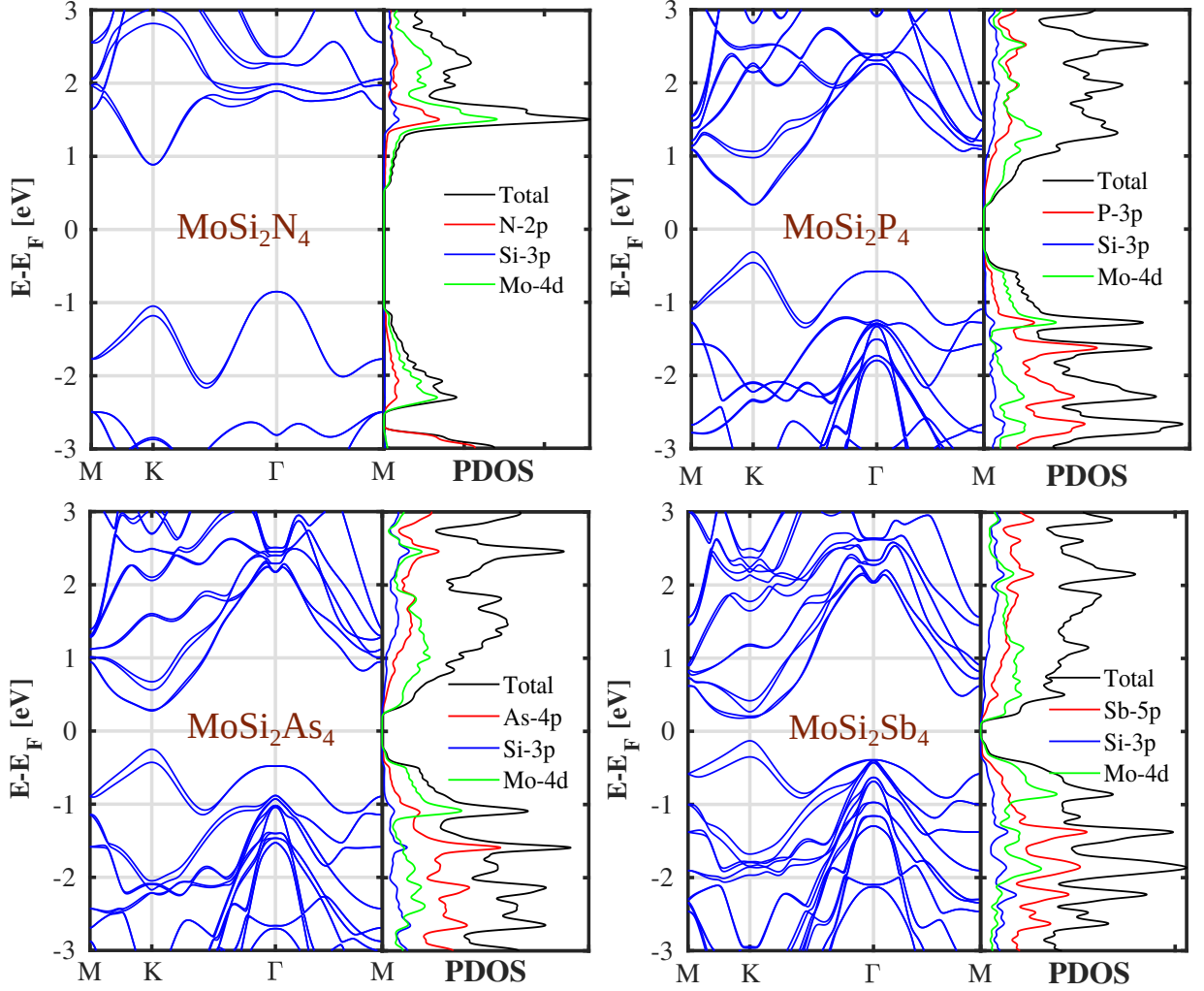


FIG. 4: The band structure along with corresponding PDOS of $MoSi_2X_4$ structures. The d-orbital of Mo atom and p-orbitals of Si and X atoms have the main contributions to the DOS.

the first and second conduction bands are listed in the table. The value of spin-splitting of $MoSi_2N_4$ at K-point ($\lambda_{K,V}$) of the valence band is 131 meV which is a little smaller than 140 meV from experimental work. However, 130 meV is reported for $\lambda_{K,V}$ in the theoretical papers³⁰. Furthermore, the calculated value of $\lambda_{K,V}$ for $MoSi_2As_4$ is 0.179 eV and in good agreement with previous reported values^{24,30}. $\lambda_{K,V}$ increases with changing X-atom from N to Sb and reaches 220 meV for $MoSi_2Sb_4$. The spin-splitting at the first conduction band ($\lambda_{K,C1}$) is not considerable. On the contrary, the second band

demonstrates a significant spin-splitting and for example, is larger than $\lambda_{K,V}$ in $MoSi_2N_4$, but the energy of the second band is much higher than the first band in this compound. The spin-splitting at K-valley in the second conduction band ($\lambda_{K,C2}$) decreases from 187 meV in $MoSi_2N_4$ to 83 meV in $MoSi_2P_4$ and increases by changing X atom from P to Sb. By looking at the conduction band of $MoSi_2As_4$ and $MoSi_2Sb_4$ at K-point, one can find that the first and third bands do not demonstrate remarkable spin-splitting, while the second and fourth display notable spin-splitting.

TABLE II: The band gap calculated with PBE functional (E_g^{PBE}) and PBE with spin-orbit coupling included (E_g^{SOC}), the energies of conduction (E_C-E_F) and valence band (E_V-E_F) edges, the compressive strain (ε_{trans}) and pressure (P_{trans}) required for semiconductor to metal transition, the spin-splitting at K point of the valence band (λ_{KV}) and first and second bands of conduction (λ_{KC1} and λ_{KC2}).

	E_g^{PBE} (eV)	E_g^{SOC} (eV)	VBM	CBM	E_C-E_F (eV)	E_V-E_F (eV)	ε_{trans} (%)	P_{trans} (GPa)	λ_{KV} (eV)	λ_{KC1} (eV)	λ_{KC2} (eV)
MoSi ₂ N ₄	1.73	1.721	Γ	K	0.582	-1.139	-22	25.3	0.131	0.003	0.187
MoSi ₂ P ₄	0.772	0.648	K	K	0.333	-0.315	-11	9.1	0.143	0.004	0.083
MoSi ₂ As ₄	0.664	0.525	K	K	0.275	-0.25	-11	8.9	0.179	0.014	0.113
MoSi ₂ Sb ₄	0.481	0.309	K	K	0.179	-0.131	-10	7.3	0.22	0.018	0.151

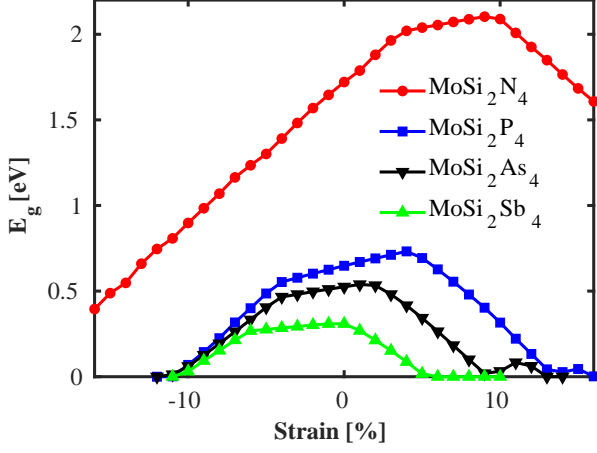


FIG. 5: The band gap variation as a function of vertical strain.

TABLE III: The effective masses at K- and Γ -points of the valence band and K-valley in the conduction band. All reported effective masses are in m_0 unit.

	$m_{K \rightarrow M}^{v,*}$	$m_{K \rightarrow \Gamma}^{v,*}$	$m_{\Gamma \rightarrow K}^{v,*}$	$m_{\Gamma \rightarrow M}^{v,*}$	$m_{K \rightarrow M}^{c,*}$	$m_{K \rightarrow \Gamma}^{c,*}$
MoSi ₂ N ₄	0.794	0.595	1.375	1.37	0.544	0.485
MoSi ₂ P ₄	0.562	0.388	1.483	1.335	0.697	0.567
MoSi ₂ As ₄	0.701	0.438	1.586	1.407	1.206	0.625
MoSi ₂ Sb ₄	0.925	0.447	2.288	1.992	1.843	0.647

The effective masses of the conduction and valence bands are reported in Table III. The effective masses of both Γ - and K-points of the valence band are presented in the table. K-point demonstrates a lower effective mass with respect to Γ -one. The anisotropic contour around K-valley leads to two different values at K to M and K to Γ paths. The K to M effective mass ($m_{K \rightarrow M}^{v,*}$) displays a higher value than K to Γ effective mass ($m_{K \rightarrow \Gamma}^{v,*}$). On the other hand, Γ -point owns isotropic contour, and effective masses at different paths are approximately equal. In Ref. 9, the effective mass of the electron is reported to be $0.486 m_0$, which corresponds to our calculated value $0.485 m_0$ for K to Γ path. Furthermore, the reported value of the hole effective mass is $0.683 m_0$ that is in the middle of our calculated effective masses at K-valley. However, Γ -point is the VBM and demonstrates a larger effective

masses. Except MoSi₂N₄, the effective masses for the valence band increase for heavier compounds and MoSi₂P₄ contains the lowest effective mass. On the other hand, only K-valley contributes to the conduction band. The effective masses at two different paths for this valley are reported in the table. The effective masses in these two paths are in the same range for MoSi₂N₄ and MoSi₂P₄, whereas their differences are enhanced for MoSi₂As₄ and MoSi₂Sb₄. As mentioned before, the contour around K-valley changes from circular for MoSi₂N₄ to triangular in MoSi₂Sb₄. In this regard, MoSi₂Sb₄ demonstrates high anisotropic effective masses at two different paths. The effective masses of the conduction band increase for the heavier compounds. MoSi₂N₄ and MoSi₂P₄ possess the lowest effective mass in the conduction and valence bands, respectively.

The vertical strain is known as a powerful tool to modify electrical and spin properties of two-dimensional compounds^{31,32}. This strain can be applied by out-of-plane pressure and 2D materials can be used as a pressure sensor. The vertical strain is applied to the four structures and their electrical and spin properties are studied. First, the variation of the band gaps as a function of vertical strain is depicted in Fig. 5. The band gaps exhibit a maximum value at a specific small tensile strain and then decrease for larger compressive and tensile strains. The band gaps vanish at transition strains (ε_{trans}). The value of compressive ε_{trans} and its corresponding pressure (P_{trans}) are reported in Table II. The band gaps of MoSi₂P₄, MoSi₂As₄ and MoSi₂Sb₄ vanish around the strain of -10% or -11%. On the other hand, MoSi₂N₄ demonstrates a higher bandgap, and ε_{trans} is two times larger at -22% strain. P_{trans} for MoSi₂P₄, MoSi₂As₄ and MoSi₂Sb₄ is in the range of [7.3-9.1] GPa, whereas MoSi₂N₄ demonstrates much larger P_{trans} of 25.3 GPa. The transition pressures for bilayers are reported from 2.18 GPa in CrSi₂N₄ to 32.04 GPa in TiSi₂N₄¹¹ that are comparable with MoSi₂X₄ monolayer. This transition pressure range also proves that applying out-of-strain to monolayer MoSi₂X₄ is feasible. The band gaps also vanish at tensile strain. MoSi₂Sb₄ demonstrates higher sensitivity to tensile strain and its band gap vanishes at lower strains. The transition strain at tensile regime increases as X atom changes from Sb to N. One can conclude from the figure that tensile transition strain of MoSi₂N₄ is

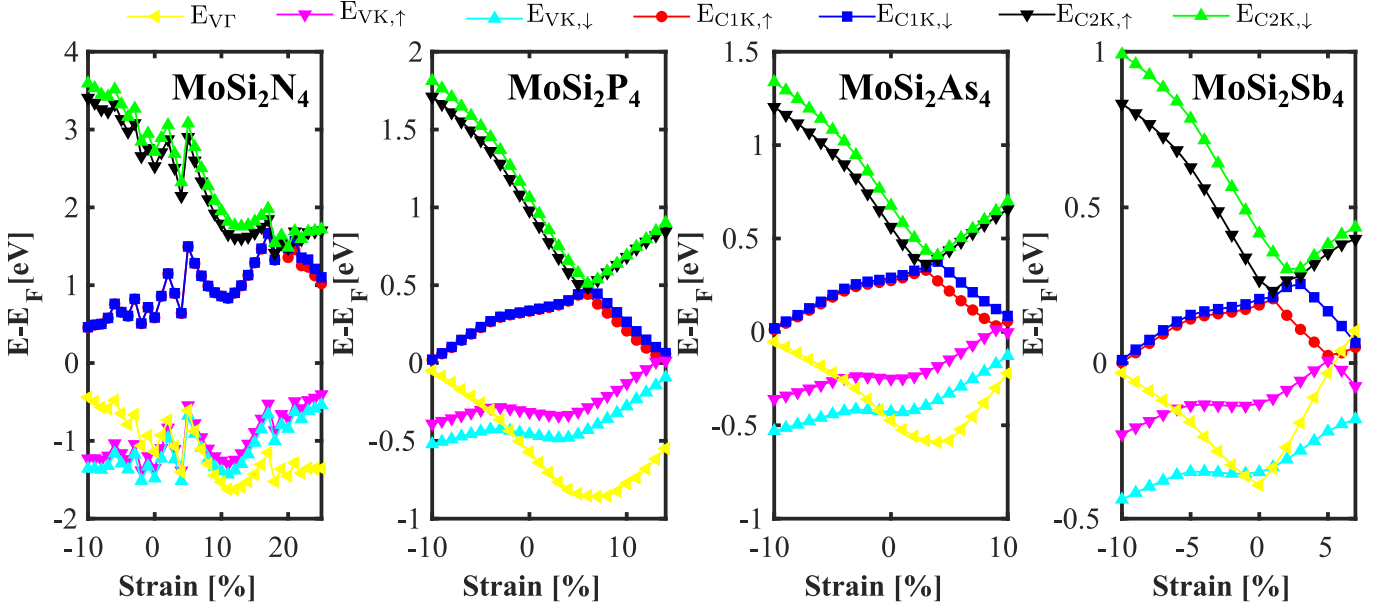


FIG. 6: The energies of the K-valleys of the first and second conduction bands along with K- and Γ -points of the valence band versus vertical strain. The up- and down-spin for each band are also indicated. The range of strain is kept in the semiconducting phase and is different for various compounds.

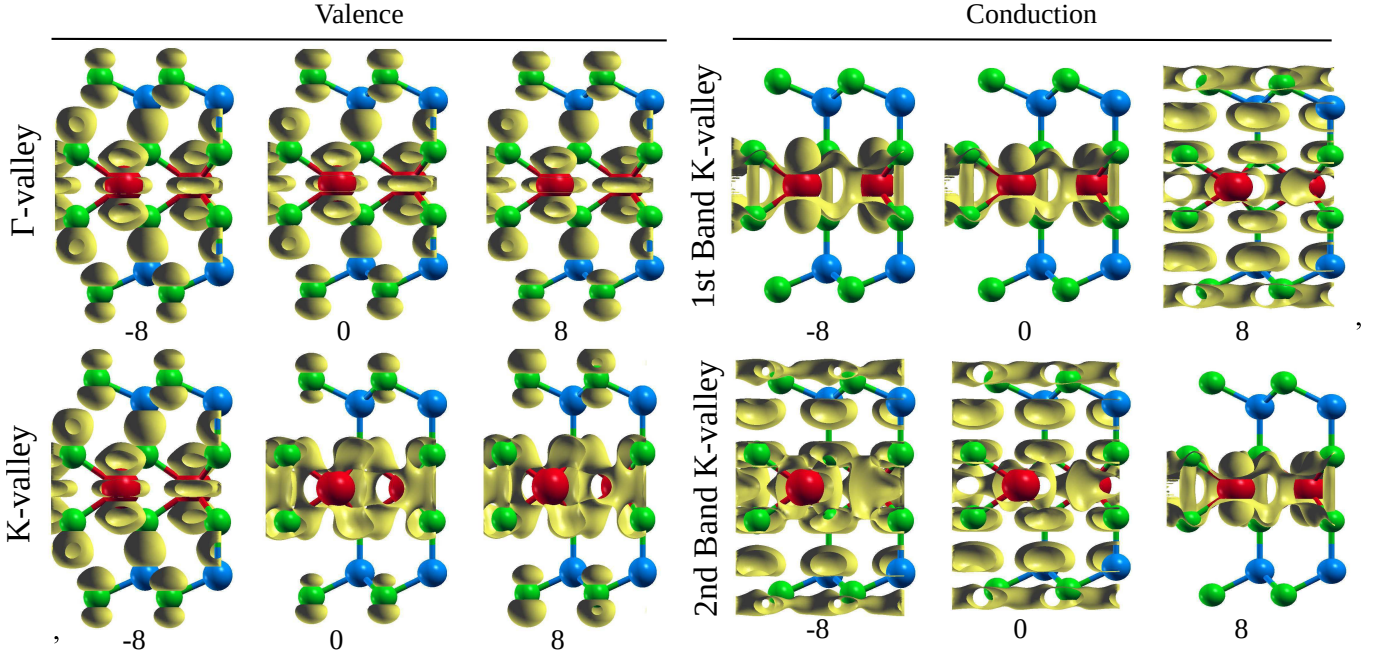


FIG. 7: Charge distribution for MoSi_2P_4 as a sample. The charge is plotted for Γ - and K-point in the valence band and for the first and second conduction band at K-valley.

much larger than 15%.

The energies of the K-valleys for the first and second conduction bands, and K- and Γ -points of the valence band versus vertical strain is plotted in Fig. 6. The energies of the up- and down-spins are separately shown in the figure. The strain ranges of the figures are different and the strain ranges are selected in the semiconduct-

ing phase. At large compressive strains, the energy of Γ -point of the valence band is higher than K-point and K-valley determines the VBM. By increasing strain from compressive to the tensile regime, the energy of Γ -point decreases, and the energy of K-point increases. One can find the large spin-splitting at K-point, whereas Γ -point does not demonstrate any splitting. On the other hand,

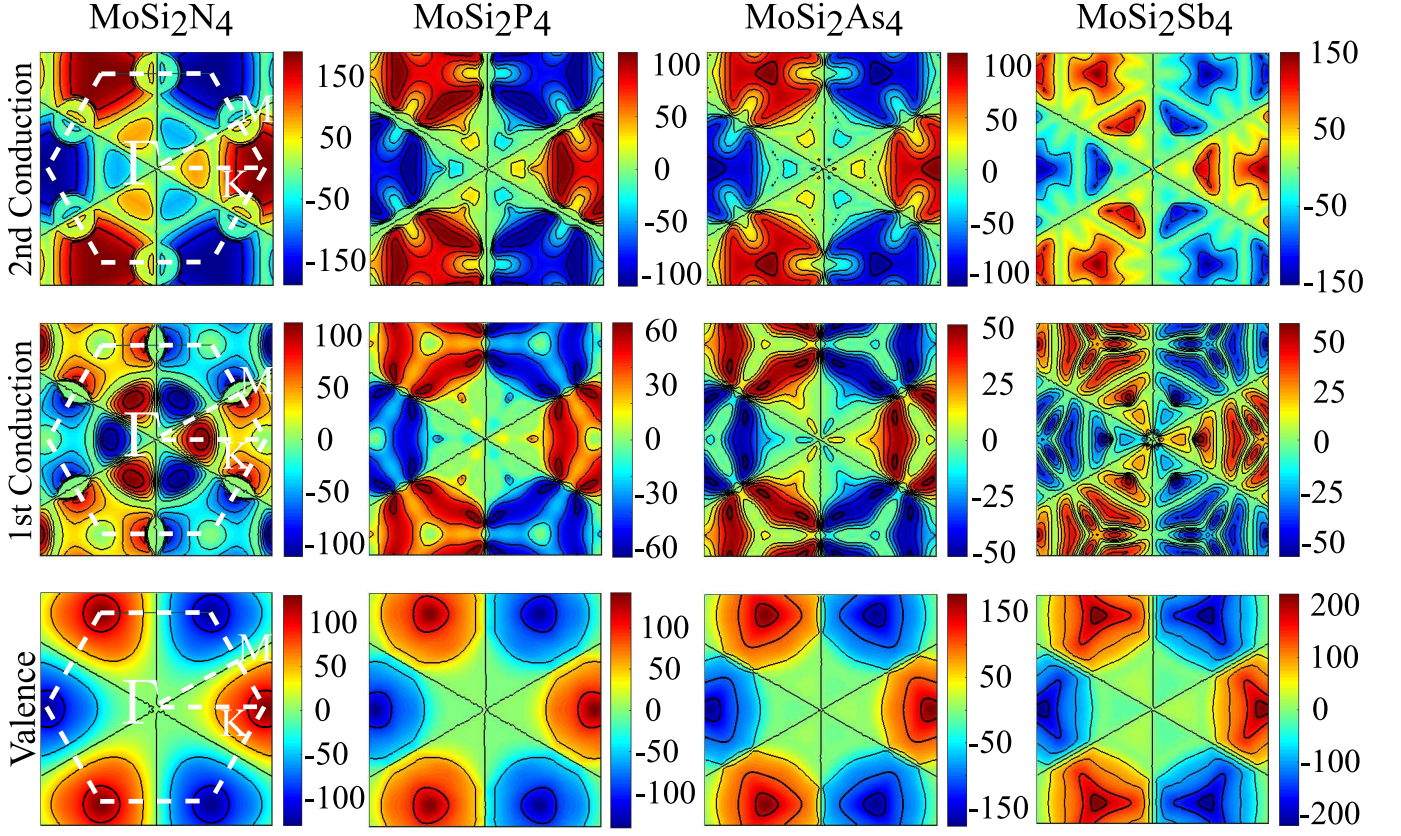


FIG. 8: Two-dimensional map of the spin-splitting in the first and second conduction bands along with valence band. The first Brillouin zone is highlighted by the dashed line in the first compound. The large spin-splitting at valence and second conduction band is obvious.

two bands contribute to the conduction band. We have called the bands with low and large spin-splitting as α -band and β -band, respectively. The α -band contributes as CBM at compressive and small tensile strains. The larger tensile strains bring down the β -band and change the location of these two bands. Therefore, CBM is contributed by β -band at a large tensile strain regime.

The charge distribution around K- and Γ -points of the valence band and K-valleys of the first and second conduction bands in the case of MoSi_2P_4 is shown in Fig. 7. A single layer of MoSi_2P_4 can be divided into three sub-layers. The charge is significantly localized around the Mo atom in the K-point of valence and conduction bands. Γ -point of the valence band has bonding character between P and Si atoms of two sub-layers. In addition, the charge is distributed around the most external P atoms. The out-of-plane strain does not significantly affect charge distribution at this point. In the K-point of the valence band, the charge is highly distributed in the internal MoN_2 sub-layer and a small charge is around outer P atoms. At compressive out-of-plane strain, the charge around outer P atoms is expanded. Furthermore, the first and second conduction bands at K-valley are compared in the figure. At equilibrium, the charge is localized in the internal sub-layer for the first band, whereas the charge is distributed in the whole thickness

of the compound for the second band. The compressive strain does not affect the charge distribution, whereas tensile strain changes the location and charge density of these two bands.

Two-dimensional maps of the spin-splitting in the first Brillouin zone for all compounds have been shown in Fig. 8. Both first and second conduction bands along with the valence band are indicated in the figure. The positive and negative spin-splitting around K and K'-valleys are obvious in the figures, respectively. The first conduction bands of all compounds except MoSi_2N_4 display a low spin-splitting. In the case of MoSi_2N_4 , a large spin-splitting is around M- and Γ -valley, but these two valleys do not contribute to the CBM. One can observe that the spin-splitting of the first conduction band is approximately zero on the boundary of the first Brillouin zone for MoSi_2P_4 and MoSi_2As_4 . On the contrary, the second conduction band exhibits a high spin-splitting which is located at K- and K'-valleys. MoSi_2N_4 and MoSi_2Sb_4 demonstrate a higher spin-splitting compared to the others. The valence band shows a tidy spin-splitting so that the splitting is maximum around K- and K'-valleys and it vanishes elsewhere. The spin-splitting increases for heavier compounds and MoSi_2Sb_4 shows the highest value. We have seen from Table II that the valence band of MoSi_2Sb_4 has the highest spin-splitting as high

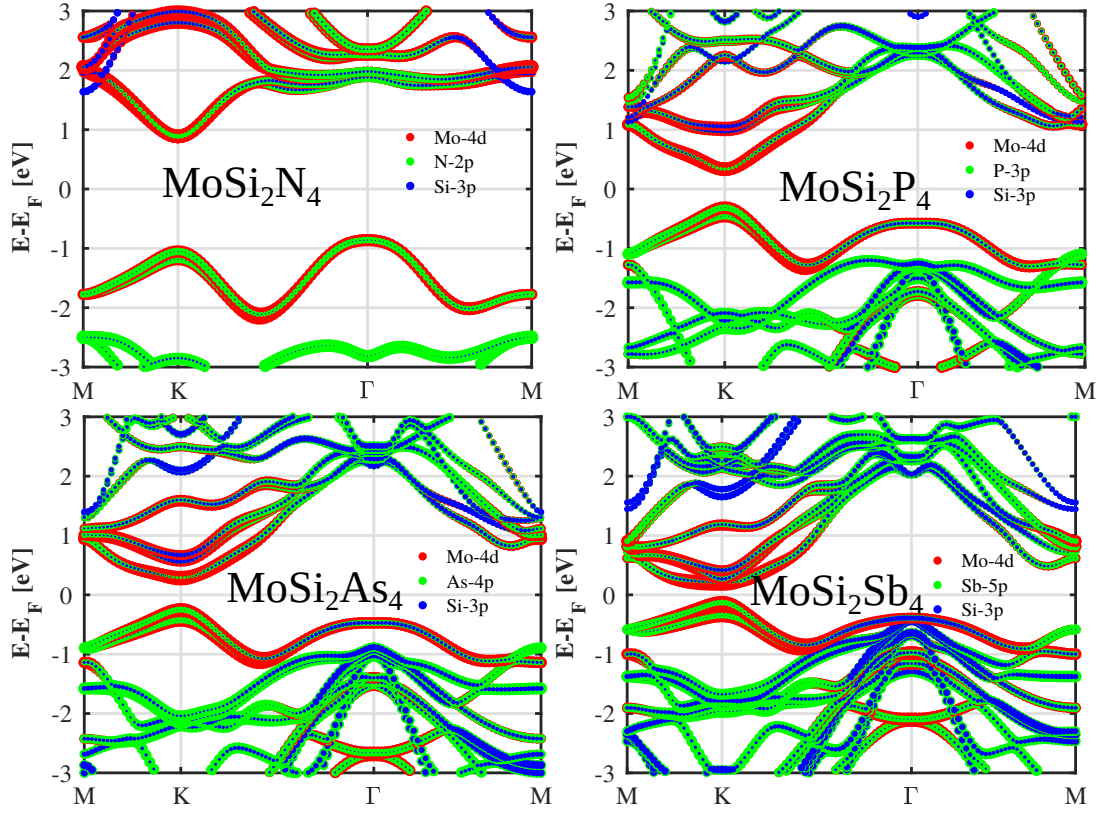


FIG. 9: Projected band structures for the studied materials. The d-orbital of Mo along with the p-orbital of Si and X atoms have the main contributions around the band gaps.

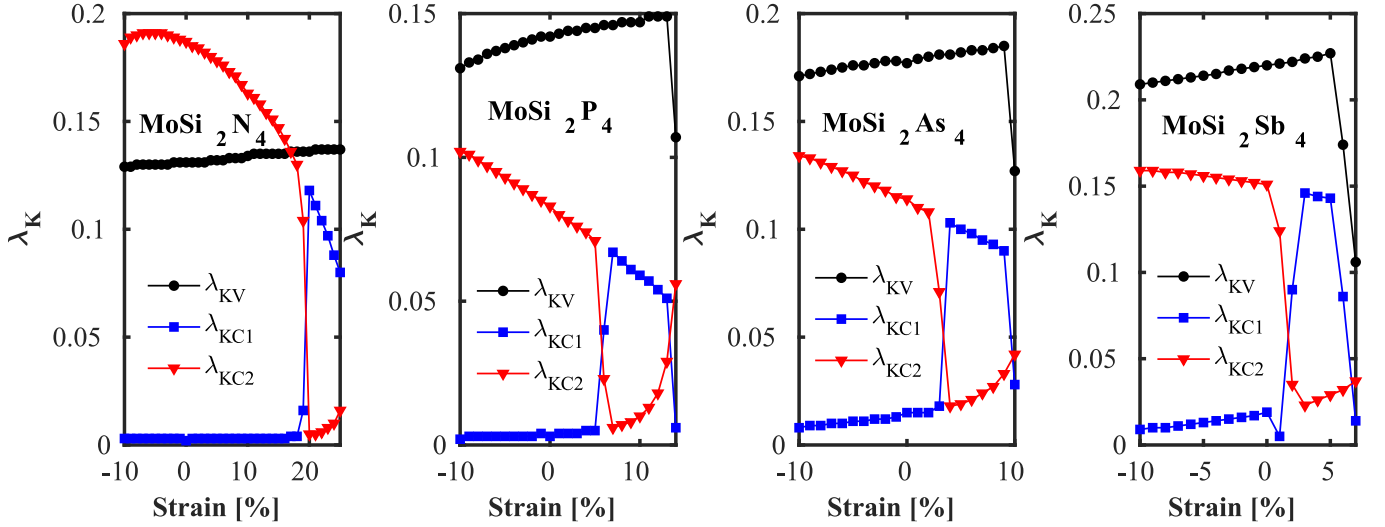


FIG. 10: The spin-splitting of the conduction and valence bands at the K-point. The valence band along with the first and second conduction bands are studied.

as 220 meV. The spin-splitting of the valence band is isotropic around the K-valley of MoSi_2P_4 and other materials specially MoSi_2Sb_4 demonstrate anisotropic spin-splitting. In this regard, the contour around the K-valley of MoSi_2P_4 is circular, whereas MoSi_2Sb_4 has a triangular shape.

To clarify the origin of spin-splitting in the valence and conduction bands, the projected band structure of four structures is plotted in Fig. 9. As it is obvious, the first and second conduction bands at K-valley are mainly affected by the d-orbitals of molybdenum atoms. The p-orbitals of X and Si atoms have a low contribution on

the first and second bands, respectively. The large spin-splitting of the second band comes from the d-orbitals, whereas the first conduction band with a high d-orbital contribution shows a small splitting. Maybe, this is related to the odd and even bands because the third one also displays a negligible spin-splitting in MoSi_2As_4 and MoSi_2Sb_4 . In addition, the valence band at K- and Γ -points is highly formed by the d-orbitals of Mo atoms. The p-orbitals of X atoms also have a considerable influence at the K-point, whereas p-orbitals of Si atoms contribute to the Γ -point. Therefore, the d-orbitals of Mo atoms, the p-orbitals of X and Si atoms have the most impact on the Γ -point of the valence band, respectively. The large spin-splitting at valence band is originated from the d-orbitals, whereas the p-orbitals of X atoms enhance the spin-splitting for heavier compounds.

The spin-splitting of the K-point of the valence band and the first and second bands of the conduction band versus vertical strain is shown in Fig. 10. $\lambda_{K,V}$ increases slightly when strain increases from compressive to tensile regime. The increase of the spin-splitting of the valence band with respect to strain has also observed in the group-III monochalcogenides³³. One can find from the band structures and Table II, that the first conduction band has a negligible spin-splitting, while the second band demonstrates a considerable spin-splitting. $\lambda_{K,C1}$ increases when strain increases from compressive to tensile, whereas $\lambda_{K,C2}$ decreases. The slope of $\lambda_{K,C2}$ variation is higher in lighter compounds. As one can observe the curves of $\lambda_{K,C1}$ and $\lambda_{K,C2}$ change with each other at the tensile strain. As we have seen in Fig. 6, the β -band moves downward and becomes lower than α -band for tensile strain. So, in the tensile regime, β -band with large spin-splitting is the first conduction band. This band changing is also observed in the figure.

IV. CONCLUSION

The electrical and spin properties of monolayer MoSi_2X_4 (X = N, P, As, and Sb) under vertical strain are investigated. MoSi_2N_4 demonstrates an indirect bandgap from Γ at valence to K at conduction band, whereas

K-valley at valence band is close to Γ -point and contributes to the valence band. On the other hand, three other compounds have direct bandgap at K-point and Γ -point at valence band is also close to K-point. Although the first conduction band demonstrates a small spin-splitting, the second conduction band has a large spin-splitting and its minimum is near to the first band. The PDOS demonstrates that the conduction and valence bands are mostly affected by the d-orbitals of Mo atoms. X atoms have a lower contribution to the valence band. The projected band structure also demonstrates that the conduction and valence bands are mainly constructed from the d-orbitals of Mo atoms. The p-orbitals of X and Si atoms also contribute to the valence and second conduction bands, respectively. The spin-splitting at K-point ($\lambda_{K,V}$) of valence band increases with changing X-atom from N to Sb and reaches 220 meV for MoSi_2Sb_4 . The spin-splitting at K-valley in the second conduction band ($\lambda_{K,C2}$) increases from 83 meV in MoSi_2P_4 to 151 meV for MoSi_2Sb_4 . In the following, the effect of vertical strain has been investigated. The band gaps exhibit a maximum value at small tensile strains, then they decrease for compressive and larger tensile strains. The band gaps close at compressive transition strains (ϵ_{trans}) of around -10% for all compounds except MoSi_2N_4 that its bandgap vanishes at the larger strain of about -22%. Transition pressures are also distributed from 9.1 to 7.3 GPa for MoSi_2P_4 , MoSi_2As_4 and MoSi_2Sb_4 , whereas MoSi_2N_4 displays a larger P_{trans} of 25.3 GPa. In addition, the charge is mostly localized around Mo atoms in both valence and conduction bands. The spin-splitting around K-valley at the valence band is isotropic and circular in the case of MoSi_2P_4 , whereas the anisotropy increases for heavier compounds and MoSi_2Sb_4 exhibits a triangular shape contour. The spin-splitting of K-valley of the valence band increases when strain increases from compressive to tensile regime. $\lambda_{K,C1}$ increases when strain increases from compressive to tensile, and at the same time, $\lambda_{K,C2}$ decreases. The slope of $\lambda_{K,C2}$ variation is higher for the lighter compounds. $\lambda_{K,C1}$ and $\lambda_{K,C2}$ change with each other at the tensile strain. In addition to the electrical properties, the vertical strain can also control the spin properties.

* Electronic address: n.ghobadi@znu.ac.ir

- ¹ A. C. Neto, F. Guinea, N. M. Peres, K. S. Novoselov, and A. K. Geim, Reviews of modern physics **81**, 109 (2009).
- ² B. Radisavljevic, A. Radenovic, J. Brivio, V. Giacometti, and A. Kis, Nature nanotechnology **6**, 147 (2011).
- ³ J. Guan, Z. Zhu, and D. Tománek, Physical review letters **113**, 046804 (2014).
- ⁴ S. Zhang, Z. Yan, Y. Li, Z. Chen, and H. Zeng, Angewandte Chemie **127**, 3155 (2015).
- ⁵ G. W. Mudd, S. A. Svatek, T. Ren, A. Patané, O. Makarovskiy, L. Eaves, P. H. Beton, Z. D. Kovalyuk, G. V. Lashkarev, Z. R. Kudrynskiy, et al., Advanced Ma-

- terials **25**, 5714 (2013).
- ⁶ Q. Li, L. He, C. Sun, and X. Zhang, The Journal of Physical Chemistry C **121**, 27563 (2017).
- ⁷ Y. Wang, S.-S. Wang, Y. Lu, J. Jiang, and S. A. Yang, Nano letters **16**, 4576 (2016).
- ⁸ B. Ozdemir, Computational Condensed Matter **17**, e00335 (2018).
- ⁹ Y.-L. Hong, Z. Liu, L. Wang, T. Zhou, W. Ma, C. Xu, S. Feng, L. Chen, M.-L. Chen, D.-M. Sun, et al., Science **369**, 670 (2020).
- ¹⁰ L. Wang, Y. Shi, M. Liu, A. Zhang, Y. Hong, R. Li, Q. Gao, M. Chen, W. Ren, H. Cheng, et al., Nature Communica-

- tions **12** (2021).
- ¹¹ H. Zhong, W. Xiong, P. Lv, J. Yu, and S. Yuan, *Physical Review B* **103**, 085124 (2021).
 - ¹² B. Li, J. Geng, H. Ai, H. Bai, K. H. Lo, K. W. Ng, Y. Kawazoe, H. Pan, et al., *Nanoscale* (2021).
 - ¹³ B. Mortazavi, B. Javvaji, F. Shojaei, T. Rabczuk, A. V. Shapeev, and X. Zhuang, *Nano Energy* **82**, 105716 (2021).
 - ¹⁴ J. Yu, J. Zhou, X. Wan, and Q. Li, *New Journal of Physics* **23**, 033005 (2021).
 - ¹⁵ A. Bafekry, M. Faraji, D. Hoat, M. Shahrokhi, M. Fadlallah, F. Shojaei, S. A. H. Feghhi, M. Ghergherehchi, and D. Gogova, *Journal of Physics D: Applied Physics* **54**, 155303 (2021).
 - ¹⁶ H. Yao, C. Zhang, Q. Wang, J. Li, Y. Yu, F. Xu, B. Wang, and Y. Wei, *Nanomaterials* **11**, 559 (2021).
 - ¹⁷ C. Yang, Z. Song, X. Sun, and J. Lu, *Physical Review B* **103**, 035308 (2021).
 - ¹⁸ H. Ai, D. Liu, J. Geng, S. Wang, K. H. Lo, and H. Pan, *Physical Chemistry Chemical Physics* **23**, 3144 (2021).
 - ¹⁹ A. P. Nayak, S. Bhattacharyya, J. Zhu, J. Liu, X. Wu, T. Pandey, C. Jin, A. K. Singh, D. Akinwande, and J.-F. Lin, *Nature communications* **5**, 1 (2014).
 - ²⁰ Z.-H. Chi, X.-M. Zhao, H. Zhang, A. F. Goncharov, S. S. Lobanov, T. Kagayama, M. Sakata, and X.-J. Chen, *Physical review letters* **113**, 036802 (2014).
 - ²¹ N. Ghobadi, *Physica E* **111**, 158 (2019).
 - ²² A. Bafekry, C. Stampfl, M. Naseri, M. M. Fadlallah, M. Faraji, M. Ghergherehchi, D. Gogova, and S. Feghhi, *Journal of Applied Physics* **129**, 155103 (2021).
 - ²³ Q. Wu, L. Cao, Y. S. Ang, and L. K. Ang, *Applied Physics Letters* **118**, 113102 (2021).
 - ²⁴ S.-D. Guo, W.-Q. Mu, Y.-T. Zhu, and X.-Q. Chen, *Physical Chemistry Chemical Physics* **22**, 28359 (2020).
 - ²⁵ J. M. Soler, E. Artacho, J. D. Gale, A. García, J. Junquera, P. Ordejón, and D. Sánchez-Portal, *J. Phys.:Condensed Matter* **14**, 2745 (2002).
 - ²⁶ J. P. Perdew and A. Zunger, *Phys. Rev. B* **23**, 5048 (1981).
 - ²⁷ A. Kokalj, **28**, 155 (2003).
 - ²⁸ S. B. Touski and N. Ghobadi, *Physica E* p. 114407 (2020).
 - ²⁹ N. Ghobadi and S. B. Touski, *Journal of Physics: Condensed Matter* **33**, 085502 (2020).
 - ³⁰ S. Li, W. Wu, X. Feng, S. Guan, W. Feng, Y. Yao, and S. A. Yang, *Physical Review B* **102**, 235435 (2020).
 - ³¹ N. Ghobadi and S. B. Touski, *Journal of Physics: Condensed Matter* (2021).
 - ³² M. Shamekhi and N. Ghobadi, *Physica B* **580**, 411923 (2020).
 - ³³ M. Ariapour and S. B. Touski, *Journal of Magnetism and Magnetic Materials* **510**, 166922 (2020).